

Coupled analysis between catenary mooring and VLFS with structural hydroelasticity in waves

Yujia Wei^{a,c}, Shuangrui Yu^a, Peng Jin^d, Luofeng Huang^c, Khaled Elsherbiny^e,
Tahsin Tezdogan^{b,*}

^a Department of Naval Architecture, Ocean and Marine Engineering, University of Strathclyde, 100 Montrose Street, Glasgow, G4 0LZ, UK

^b Department of Civil, Maritime and Environmental Engineering, School of Engineering, University of Southampton, Boldrewood Innovation Campus, Building 176, Southampton, SO16 7QF, UK

^c Division of Energy and Sustainability, Cranfield University, Building 52, Cranfield, 45 College Rd, Cranfield, MK43 0AL, UK

^d School of Marine Science and Engineering, South China University of Technology, Guangzhou, 511442, China

^e Department of Marine Engineering, College of Engineering and Technology, Arab Academy for Science, Technology and Maritime Transport, Abu Quir Campus, Alexandria, Egypt

ARTICLE INFO

Keywords:

Hydroelasticity
Very large floating structure
Hydro-elastic-moored
Multi-bodies dynamics
Fluid-structure interaction

ABSTRACT

The rapid growth of marine renewables has led to the development of very large floating structures (VLFS) that are designed to operate in deep seas. It is significant to understand the mechanism of the coupled effects between deformable VLFS and catenary mooring system. This paper presents a time-domain hydro-elastic-moored model developed by integrating a quasi-static mooring module into a fully coupled Computational Fluid Dynamics (CFD) - discrete-module-beam (DMB) approach. The model is used to investigate the coupled effects between structural hydroelasticity and loose-type mooring systems on a deformable VLFS in waves. The mooring and hydroelasticity codes are validated separately and show favourable agreement with other numerical and experimental results. Then the coupled effects between the mooring system and structural hydroelasticity are evaluated by assigning various design parameters, i.e., VLFS structural stiffness and mooring stiffness. The numerical results, including dynamic motions, longitudinal vertical bending moments (VBMs) and mooring tension forces are presented and analysed. These results can be used to design a VLFS with mooring in medium-deep sea, and help with the conventional mooring design for a less-stiffness VLFS due to hydroelastic response.

1. Introduction

Very large floating structures (VLFSs) offer several advantages, including environmental friendliness, low cost, good mobility, and short construction periods, making them widely used in the maritime industry. Their potential as developable land around coastal cities for residential, industrial, and logistic purposes has been extensively studied [1]. For instance, there were projects delivered using VLFS as floating airports and cities between 1995 and 2000 (Ohmatsu, 2005), as well as concepts proposing the use of VLFS for large floating farms and floating ecopolis [2]. However, due to the large scale of such structures, their elastic deformations under wave excitations become prominent than rigid-body motions. Therefore, to accurately predict the deflection and stress distribution of VLFSs

* Corresponding author.

E-mail address: T.Tezdogan@soton.ac.uk (T. Tezdogan).

while considering environmental excitations, it is necessary to perform hydroelastic analysis during the design phase.

In recent decades, many researchers have presented studies on the hydroelasticity of VLFS with various environmental conditions. The experimental studies were conducted by Refs. [3–5]. In parallel, several numerical studies have been presented based on a partitioned fluid structure interaction (FSI) approach to investigate on the elastic deformation of the VLFS in waves. The data communication between the fluid and structure solver is accomplished through the FSI framework. Various FSI frameworks have been established in the literature by combining different fluid and structural solvers. To name a few, potential flow theory coupled with finite element method (FEA) has been established by Refs. [6,7], and potential flow coupled with multi-body dynamic method (MBD) has been established by Refs. [8,9].

Limitations arise from the potential flow theory, which does not take into account fluid viscosity. For FSI problems, the complex flow behaviours can only be accurately simulated by CFD methods. Thus, the fully nonlinear CFD method is commonly used as an alternative. It can also be coupled with a structural solver to study the elastic behaviour of a floating barge in waves, for an example, coupled CFD and FEA to a very flexible barge [10].

The mooring design of a VLFS is necessary for stabilising the structure apart from wave drifts. Various types of mooring systems can be used for VLFS, including tension leg, taut line, and catenary mooring lines. However, the specific mooring system design will depend on a range of factors such as water depth, environmental conditions, and the specific design of the VLFS. When placing the VLFS towards the intermediate-deep sea, loose-type mooring lines are mostly used, such as taut legs and catenary type of moorings. These types of mooring use weight to stabilise the structure and hang between the fairlead and anchoring. Catenary mooring has a part of the mooring line lying down on the seabed, which means the seabed effects must be considered as well.

The attachment of a loose-type mooring system to the VLFS will alter the original load distributions of the structure due to the added weight from the mooring lines. In such circumstances, the coupling effects between the structural hydroelasticity and mooring kinematics should be taken into account.

Efforts are underway to consider the influence of mooring dynamics on the structural hydroelasticity of VLFS with low rigidity. Researchers have explored a range of configurations, from two-body articulated mooring system [11], to multi-body-beam setups [6]. [12] investigated the effectiveness of vertical mooring lines in reducing the hydroelasticity of the VLFS in various incident wave angles and wavelengths using a hybrid Finite element (FE) – Boundary element (BE) method. The stiffness of the mooring lines is optimised for maximum reduction of hydroelastic responses by using differential evolution algorithm. [13] studied the coupled effects of a modular type of VLFS with the catenary type of mooring system. However, the VLFS structure used by the authors had a large stiffness, so the elastic deflections had limited effects in their cases. The authors concluded that the hydroelasticity becomes more important for those VLFS structure with less stiffness. [7] studied the effects of tension leg types of mooring lines on a very-large floating structure. They concluded that the hydroelasticity effect leads to larger vertical responses and mooring tensions compared to the rigid-body case, and the maximum mooring tension of the elastic case is 1.5 times higher than that of rigid body. [14] found that increasing mooring stiffness can reduce the vertical motion and bending moments of the structure. [15] studied the dynamic behaviour of a moored articulated floating structure in waves using AQWA. They found that the mooring stiffness has a great influence on structural motions, leading to high stress on the connection components of the modular structure. This poses an important design criterion for VLFS.

As a matter of fact, the studies on the coupled structural hydroelasticity and loose-type mooring system are rare in the open literature. Some pioneer work has highlighted the importance of understanding the mechanics of such hydro-elastic-moored systems. [13] investigated the impact of the structural elastic deflection on mooring tension using a coupled time domain potential flow method. The authors noted that the high-frequency elastic deflection may have an impact on the fatigue performance of mooring lines which necessitates further research.

To fill the gap mentioned above, a mooring module is integrated into the coupled CFD-DMB framework, forming a coupled hydro-elastic-mooring system. This framework is applied to investigate the interactive effects between the hydroelastic behaviour of a deformable VLFS and two types of mooring lines in waves. The performance of various configurations of hydro-elastic-moored flexible floating structures is also compared to that of the corresponding configuration with a rigid body assumption.

The rest of this paper is organised as follows: Section 2 presents the numerical methodologies, governing equations, and detailed model setups. Section 3 presents the verification and validation studies of the catenary mooring system, including the comparison of numerical results (rigid body motions, and line tension forces) with previous works. In Section 4, we first study the flexible behaviour of an un-moored VLFS in waves with different structural stiffness. Then the couple effects between structural hydroelasticity and the mooring system are evaluated separately. Results from this evaluation consider the coupled effects of changing mooring stiffness on structural behaviour and structural stiffness on mooring tension forces. The conclusions and future recommendations are drawn in the final section.

2. Numerical methodology

This study first integrates the quasi-static mooring solver into a two-way FSI framework to investigate the coupling effects between the structural hydroelasticity and catenary mooring lines of a VLFS in waves. The FSI framework is CFD-based, which includes an open-source CFD toolbox OpenFOAM v2012, a structural solver MBDyn-v1.73 and an in-house data communication tool. This section illustrates the main features of the fluid, solid, and mooring solvers, as well as the coupling method used.

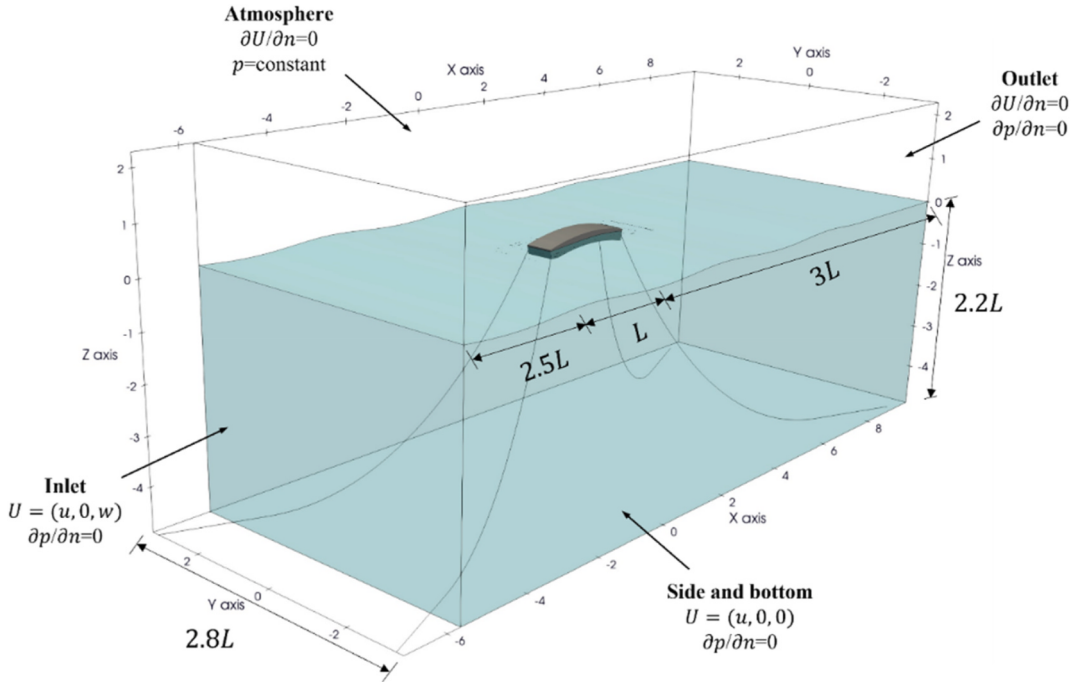


Fig. 1. Computational domain and boundary conditions.

2.1. CFD model

2.1.1. Governing equations

A multi-phase solver in OpenFOAM is applied to simulate fluid flow. In this model, the flow is assumed to be an incompressible and viscous, governed by the continuity and momentum equations presented below:

$$\nabla \cdot U = 0 \quad (1)$$

$$\frac{\partial \rho U}{\partial t} + \nabla \cdot (\rho(U - U_g)) = -\nabla P_d - g \bullet x \nabla \rho + \nabla(\mu_{eff} \nabla U) + (\nabla U) \bullet \mu_{eff} + f_\sigma \quad (2)$$

where U is the velocity of flow field and ρ is the mixed density of water and air. U_g denotes the speed of the motion of the mesh grid, g is the gravity acceleration, P_d refers to the dynamic pressure, μ_{eff} is the effective dynamic viscosity, f_σ is the surface tension which is only considered at the free surface.

The Volume of Fluid (VOF) method [16] is adopted to simulate the free surface in the numerical domain by solving an additional transport equation for the scalar quantity, a , which represents the volume fraction of fluid for each cells.

$$\frac{\partial a}{\partial t} + \nabla \bullet [(U - U_g)] a + \nabla \bullet [U_r(1 - a)a] = 0 \quad (3)$$

where U_r is the artificial compressive velocity which only functions near the free surface due to the inclusion of $(1 - a)a$.

In the multi-phase flow problem, the volume fraction of each phase was used as the weighting factor to calculate the mixture properties. The equations for the density and the viscosity can be expressed by:

$$\rho = a\rho_w + (1 - a)\rho_a \quad (4)$$

$$\mu = a\mu_w + (1 - a)\mu_a \quad (5)$$

where subscripts w and a represent the water and air phases, respectively.

To generate waves, the open-source wave generation library Waves2Foam [17] is applied to the OpenFOAM toolbox. This library generates incident waves by specifying free surface elevation and velocity distribution at the boundary inlet. The wave absorption relies on the relaxation zone technique, which provides better wave quality near the inlet boundary and removes spurious reflection at the outlet boundary. These methods have been proven to be very effective in previous studies [18]. In this study, Stokes 2nd order wave theory is applied to represent the incident waves throughout all cases.

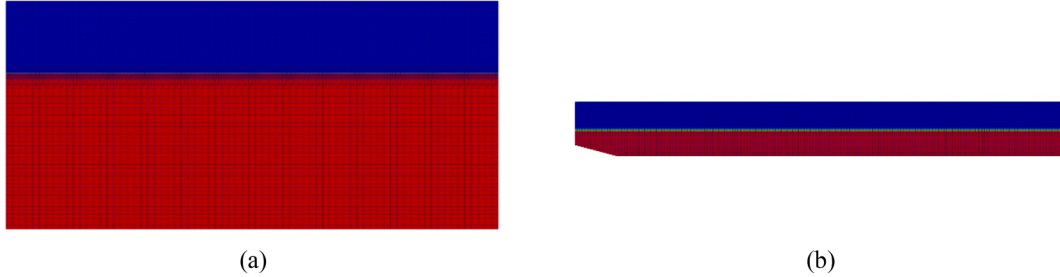


Fig. 2. Mesh refinement (a) near the free surface, (b) on the VLFS surfaces.

2.1.2. CFD configurations

The wave domain is established in the CFD computations to simulate VLFS operating in heading waves. The domain is extended in three dimensions, i.e., $-3L < x < 3.5L$, $-1.4L < y < 1.4L$ and $-2.2L < z < 1L$, where L refers to the VLFS length between perpendiculars (2.28 m). A general view of the wave domain (for the ratio of the wavelength to the structure length of $\lambda/L = 1.2$) is shown in Fig. 1. As can be seen the side boundaries are placed far away from the VLFS sides to reduce the influence of wave reflection from numerical boundaries. Inside the numerical domain, the global Cartesian coordinate system is set at the same height level with the calm water surface, coinciding with the VLFS' centreline. Two sets of computational mesh are generated, using 3.85 M cells for wave frequency between $\omega_s = 3.92 \text{ rad/s}$ to 6.28 rad/s . Another set of mesh using 5.12 M of mesh to simulate short wave with wave frequencies lower than $\omega_s = 3.92 \text{ rad/s}$. The mesh refinement is achieved near the free surface, as shown in Fig. 2(a) and the mesh sizes far from the surface layer are set larger to speed up overall computational time. Apart from the surface area, the mesh around VLFS is also refined as plotted in Fig. 2 (b).

2.2. DMB model

2.2.1. Governing equations of flexible body

This study employs MBDyn as the structure solver, which utilises a Lagrange multiplier or redundant coordinate set formation to model a multibody system. Unlike the reduced coordinate set method, which uses a minimum number of degrees of freedom (DoFs) to describe motion, the redundant formulation enforced by Lagrange multiplier [19] allows for 6 DoFs motion for each body and constraint.

The Newton-Euler equations of motion were established for each body of the system in the differential-algebraic form. This results in a set of first-order equations together with the constraint equations, forming a system of Differential-Algebraic Equations (DAE) as follows

$$M\dot{x} = P \quad (6)$$

$$\dot{P} + \varphi_x^T \lambda = f(x, \dot{x}, t) \quad (7)$$

$$\varphi(x, t) = 0 \quad (8)$$

where M denotes the inertia matrix of the rigid body, x denotes the translational and rotational parameters in the global reference frame. P refers to the momentum of the body. λ denotes the vector of the Lagrange multipliers for the constraints; f is the external force and moment vector exerted upon the body which might be related to its displacement and velocity as well as time. φ is a set of kinematic constraints applied on the body and φ_x^T is the Jacobian of φ with respect to the generalised coordinate.

To consider the effects of structural deformations, the distance between each two adjacent nodes is treated as a Euler-Bernoulli beam. In the present study, a three-node beam element using the Geometrically Exact Beam Theory (GEBT) [20] is implemented in the MBDyn software through a finite volume approach for the multibody formulation of three-node beam elements. The internal forces and moments are evaluated at the evaluation points, and the constitutive law is used to calculate the geometrical strains and curvatures based on the following equations.

$$\begin{Bmatrix} F_x \\ F_y \\ F_z \\ M_x \\ M_y \\ M_z \end{Bmatrix} = f \left\{ \begin{Bmatrix} \varepsilon_x \\ \gamma_y \\ \gamma_z \\ \kappa_x \\ \kappa_y \\ \kappa_z \end{Bmatrix}, \begin{Bmatrix} \dot{\varepsilon}_x \\ \dot{\gamma}_y \\ \dot{\gamma}_z \\ \dot{\kappa}_x \\ \dot{\kappa}_y \\ \dot{\kappa}_z \end{Bmatrix} \right\} \quad (9)$$

where F_x is the axial force component, F_y and F_z are the shear force components, M_x is the torsional moment component, M_y and M_z denote bending moment components; ε_x , γ_y and γ_z are the axial strain and shear strain coefficients, κ_x , κ_y and κ_z are the bending curvature parameters, and f is an arbitrary function of beam material constitutive law.

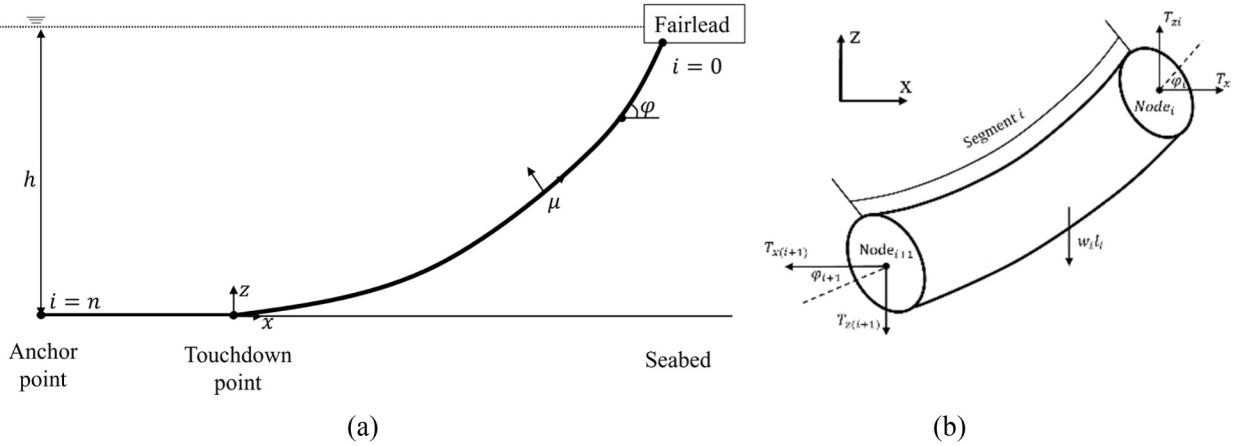


Fig. 3. (A) Catenary mooring line layout, (b) An example of small segment of mooring lines.

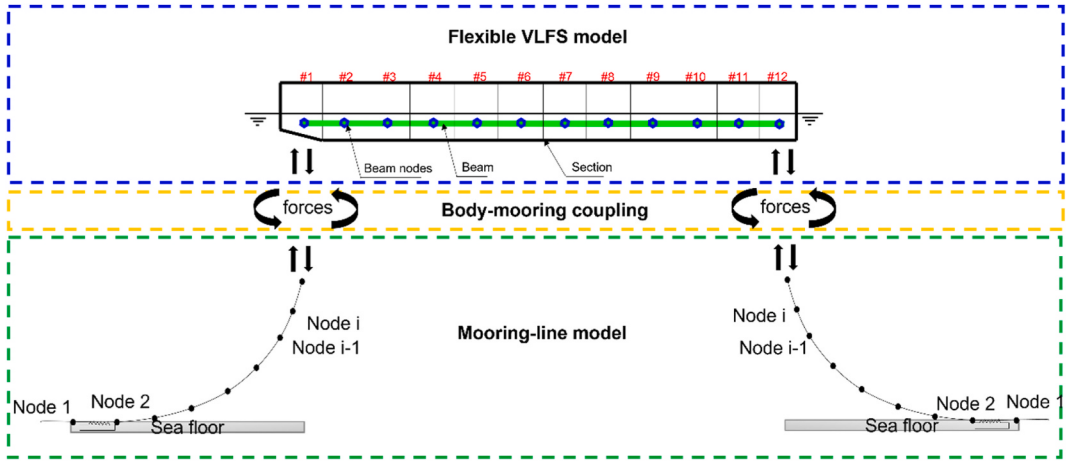


Fig. 4. Coupled DMB and catenary mooring model demonstration.

2.2.2. Governing equation for catenary mooring lines

The mooring tension is calculated using the catenary equation, derived from Ref. [21]. Fig. 3(a) shows the profile of a two-dimensional mooring line. The water depth, or the depth of the anchor point, is h . Quasi-static methods assume that the shape and tension of a mooring line at any given instant are static while ignoring the dynamic loadings from fluids.

The catenary mooring line is discretised into n segments, with a total of $n + 1$ nodes, which are numbered from 0 (fairlead) to n (anchor). For each segment, only tension force and weight in water are considered. A segment is taken as representing as shown in Fig. 3(b). In the absence of fluid forces, it is possible to resolve the equivalent forces acting normally and tangentially to the element with the following equations:

$$T_{xi} = T_{x(i+1)} \quad (10)$$

$$T_z - w_i l_i = T_{z(i+1)} \quad (11)$$

where, i denotes i^{th} segment, T_i is the total tension force at segment i which equals to the sum of horizontal and vertical components of tension forces $T_i = \sqrt{T_{xi}^2 + T_{zi}^2}$, w_i is submerged weight per unit length, l_i denotes the unstretched length of the segment.

When the segment is stretched, the tension force on the segment is calculated using [22]:

$$s_i = l_i \left(1 + \frac{T_i}{E_i A_i} \right) \quad (12)$$

where s_i denotes the stretched length of the segment, E_i is the Young's modulus and A_i is the cross sectional area of the segment.

Therefore, the geometrical constraints can be applied between the stretch segment length and the node coordinates:

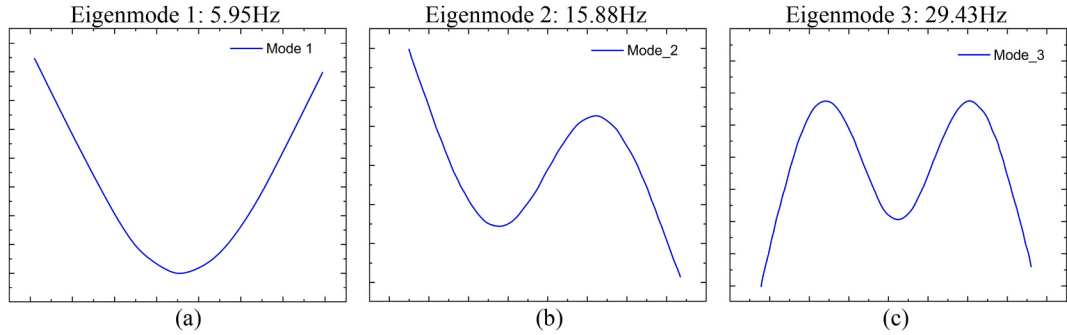


Fig. 5. Modal analysis (a) 2nd, (b) 3rd, (c) 4th orders of vertical bending.

Table 1
Eigenvalues of the flexible VLFS up to 4th order and compared with FEA.

Mode	MBDyn (Hz)	FEA (Hz)	Error (%)
2-node	5.95	6.01	0.99
3-node	15.88	16.43	3.35
4-node	29.43	32.00	8.03

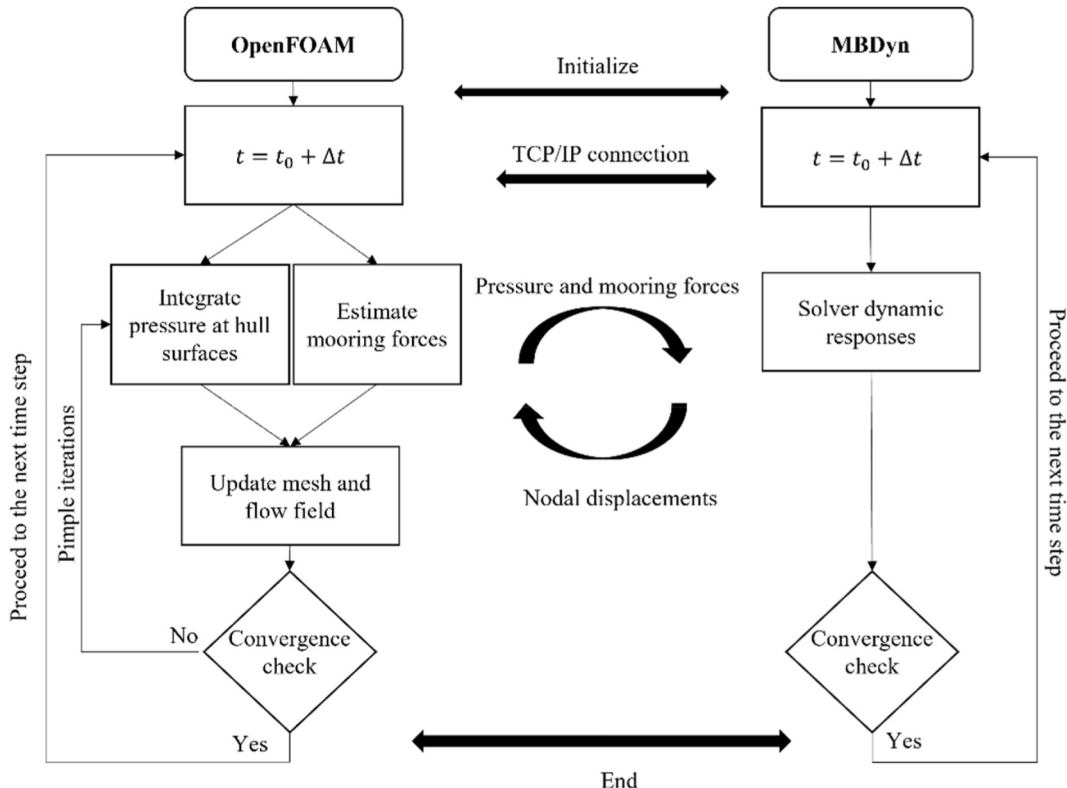


Fig. 6. The numerical framework of the hydro-elastic-moored layout.

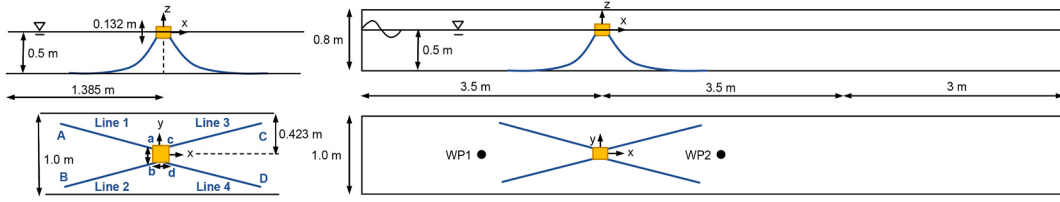


Fig. 7. The layout of the floating box with four catenary mooring lines in waves [24].

$$s_i \cos \varphi_i = x_{i+1} - x_i \quad (13)$$

$$s_i \sin \varphi_i = z_i - z_{i+1} \quad (14)$$

where φ_i is the relative angle between T_i and T_{i+1} , x and z are the horizontal and vertical coordinates of a mooring node.

The tension forces and coordinates of each node of a mooring line can be solved using Eq. (14) based on a piecewise manner. It initially starts from solving the fairlead node loads T_0 using the pre-defined coordinates x_0 and z_0 , iteration with the above procedure, update the forces and coordinate of each nodes, until it reaches to the anchor point.

For mooring line with catenary shape, a portion of line lies on the seabed and special treatment is required to handle the interaction between the mooring line and the seabed. The touchdown point is searched out when its vertical position is below the seabed ($z_i = z_{\text{anchor}}$), then the vertical tensional force T_{zi} at the touch-down point node and the nodes lied down the seabed are directly set to zero. The spring-damper system is applied to the lie-down portion of mooring lines, providing a force-displacement relationship by utilising the spring stiffness and damping coefficient to simulate the seabed effects.

2.2.3. DMB configurations

A discrete module beam model (DMB) in conjunction with a multi-segment partitioning technique is employed in MBDyn to formulate the structural models of the flexible VLFS model. The development of such a beam model has been validated for ship hydroelasticity on a S175 containership in the authors' previous papers [23] and [18].

To demonstrate a deformable structure, the surface patch of VLFS is divided into 12 sections, each section is served as a structural node and attached with a body element, as shown in Fig. 4. It is seen that a series of 11 beam elements, equivalently representing the structure's stiffness, are employed to connect the neighbouring body elements. The beam model restraints in torsional and horizontal bending effects, therefore the total-joint type of elements are applied. A number of 23 total joints are used to connect the beginning node with every other node, imposing constraints, where the free-free beam is permitted only deformed in vertical direction. Another set of total joint element is applied between the midship node and the background node to suspend the surge motion of ship beam from the drift force. As a result, the DMB beam design in this study is allowed to have heave and pitch motions and experience the vertical bending effects.

The elastic mode shapes up to 4th order, i.e., 2nd, 3rd, 4th vertical bending behaviours of the flexible VLFS are displayed in Fig. 5, and the eigenvalues are summarised in Table 1. Furthermore, the eigenvalues are compared with the finite element analysis (FEA) results presented in Ref. [10], demonstrating favourable agreement.

Catenary mooring lines are equipped to connect flexible structures to the sea bed, providing soft restraints to stabilise the deformable structure from wave drifts, as shown in Fig. 4. Within the numerical demonstration, fairlead positions are predefined on the prescribed flexible structure sections, i.e., fairleads are tied to the front section (#1) and the end section (#12) in this study. Therefore, the motions of the fairlead sections will be computed by taking into account the fluid forces (Navier-Stokes equations), Euler-Bernoulli beam equations, and catenary mooring line equations. For sections without mooring lines attached, they will only experience fluid forces and restraints from other beam nodes.

The well-established FSI framework, illustrated in Fig. 6, enables the investigation of hydroelastic behaviours in wave conditions for a hydro-elastic-moored model, while taking into account the two-way communication between the flexible structure and catenary mooring lines. In each time step, the surface pressure and mooring forces on VLFS sections are calculated using OpenFOAM and transferred to MBDyn. The MBDyn solver provides the instantaneous structural position and velocity, which are then transmitted to the CFD model to update the fluid meshes, and to the mooring models for calculating fairlead kinematics.

3. Validation of the numerical model

3.1. Floating object with mooring lines

The validation study aims to examine the performance of the catenary type of mooring lines of the present OpenFOAM code. The numerical study is conducted based on a single rigid floater with four catenary mooring lines. The mooring lines are solved using the quasi-static method. The modelling settings, including the computational domain, mesh discretisation, and numerical scheme, follow those used by Ref. [24], as shown in Fig. 7. The overset mesh method, which accounts for the floating body motions, is used as the mesh motion solver in OpenFOAM. The vertical motions of the floater (surge, heave and pitch) and the tension forces (horizontal drag forces from Line 1 and Line 3) are measured under two regular heading waves with periods of $T = 1.8\text{s}$ and 2.0s (see Fig. 8). The catenary

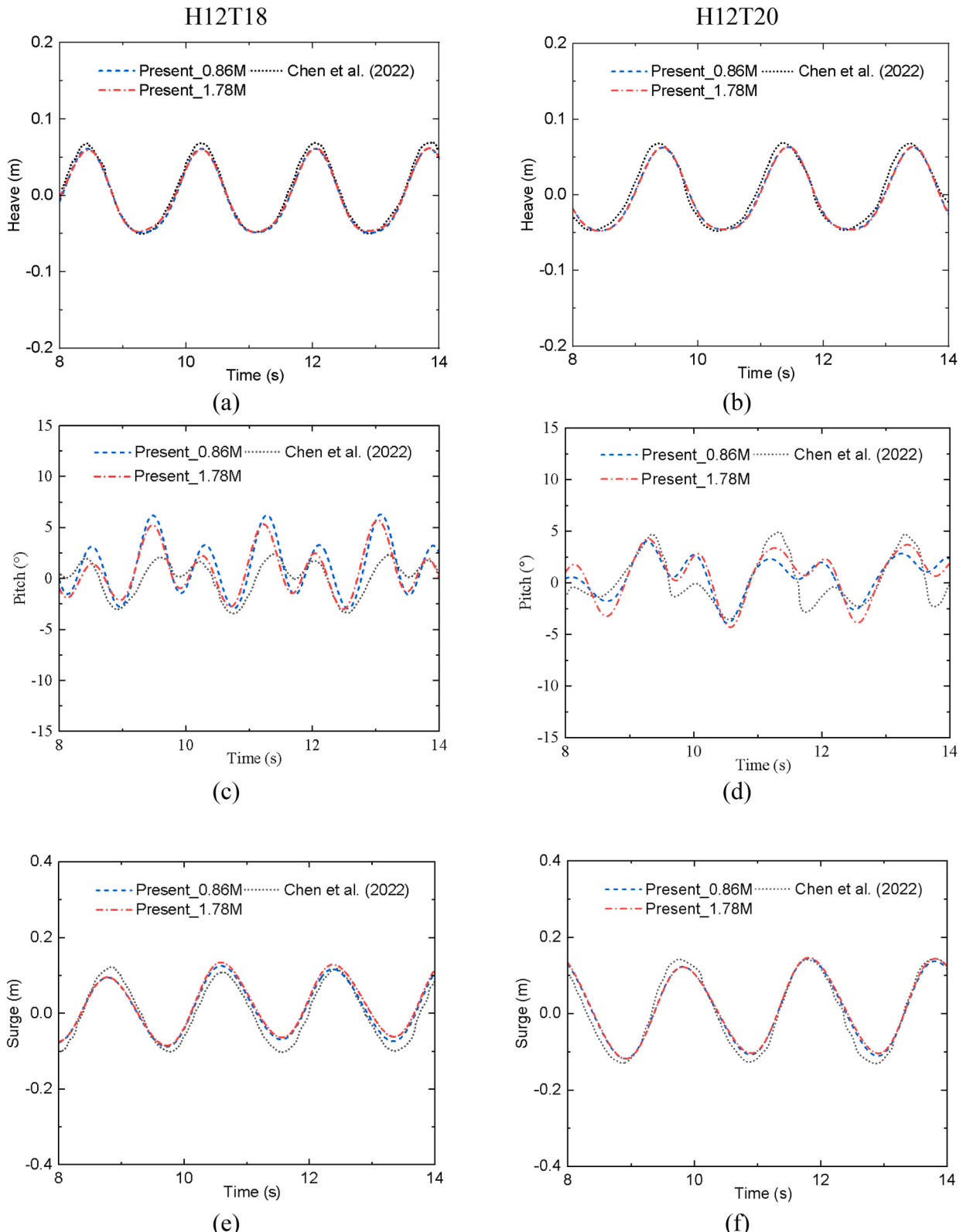


Fig. 8. Floating box motion (first row: heave; second row: pitch; third row: surge) for two regular wave cases H12T18, H12T20. Red solid lines: present mooring codes with 0.86 M cell; Green dash-dot lines: present mooring codes with 1.78 M cells; Blue dashed lines: results from Moor-Dyn [24].

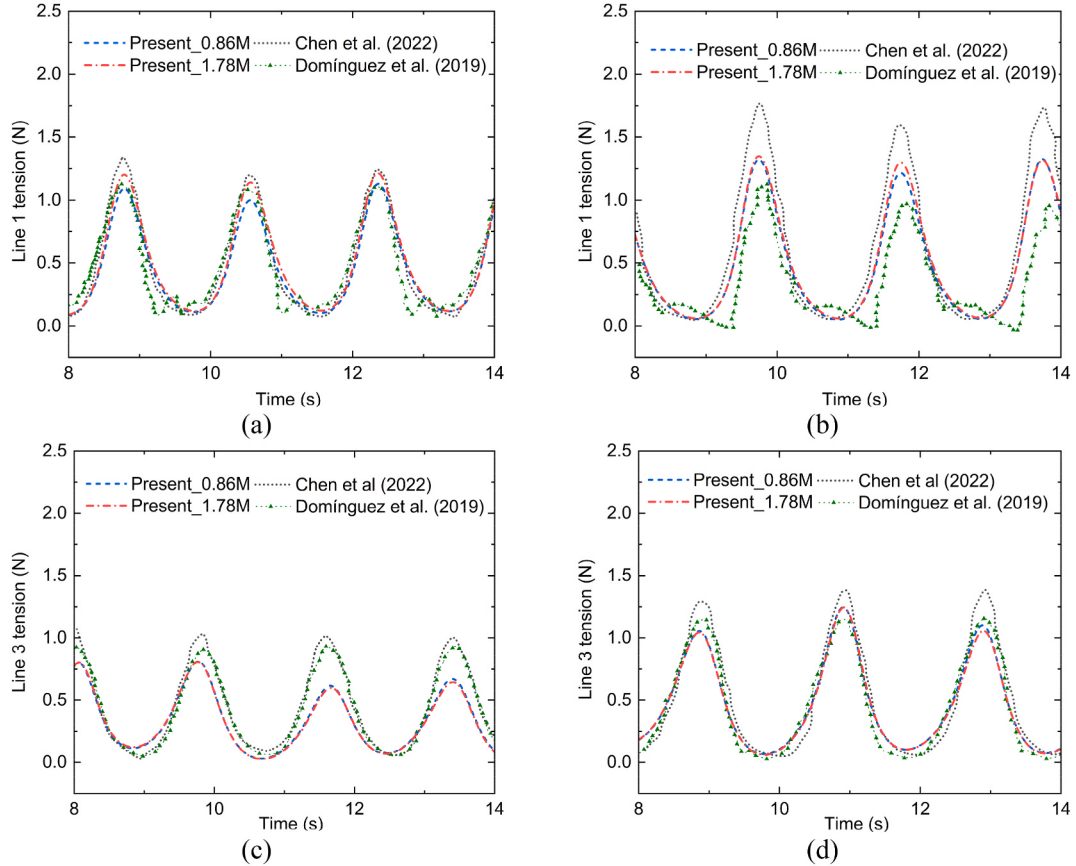


Fig. 9. Mooring tension forces (first row: Line 1; second row: Line 3) for two regular wave cases H12T18, H12T20. Red solid lines: present mooring codes with 0.86 M cell; Green dash-dot lines: present mooring codes with 1.78 M cells; Blue dashed lines: results from MoorDyn [24], Green scatter: results from experiments [25].

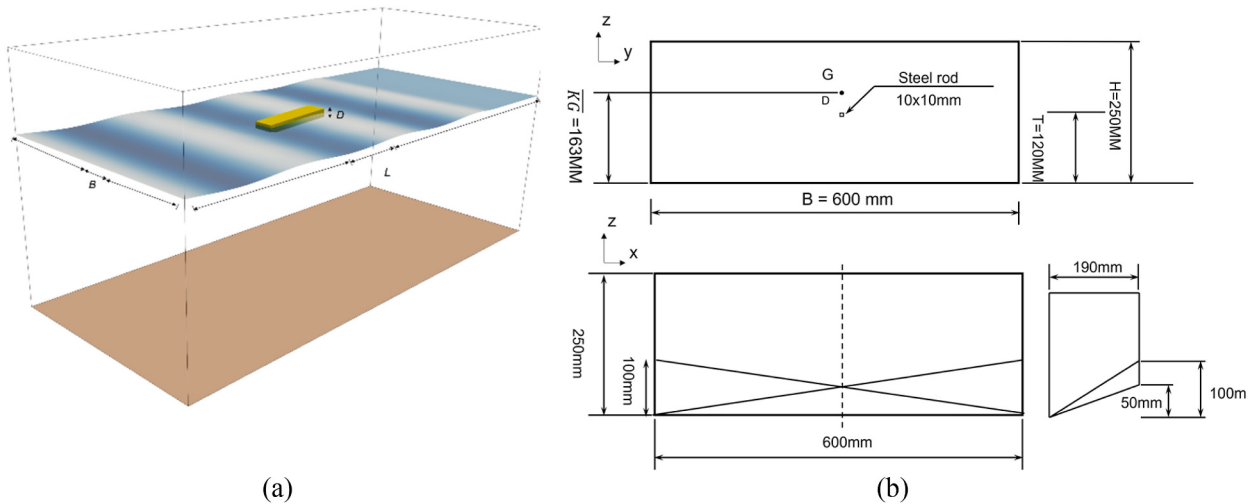


Fig. 10. VLFS geometry configuration (a) The placement of the VLFS in wave domain, (b) The geometrical properties of the VLFS.

mooring lines have a diameter of 3.656 mm and a length of 145.5 cm. The axial stiffness is 19 N/mm and the mass per unit length is 0.607 g/cm. Each mooring line is discretized into 40 segments. The internal damping coefficient is set to achieve a damping ratio of 80%. The added mass coefficient is 1.0 in the transverse direction and zero in the axial direction. The drag coefficient is 1.6 in the

Table 2
VLFS physical properties.

VLFS physical properties (unit)	Values
Length L (m)	2.28
Beam B (m)	0.6
Depth D (m)	0.25
Draft T (m)	0.12
Total mass (kg)	171.77
Length of each section (m)	0.19
Mass of each caisson (kg)	13.7 (Bow:10)
Moment of inertia of rod (m^4)	8.33×10^{-10}
Young's modulus of rod (N/ m^2)	2.1×10^{11}
Bending stiffness of the rod (N m^2)	175

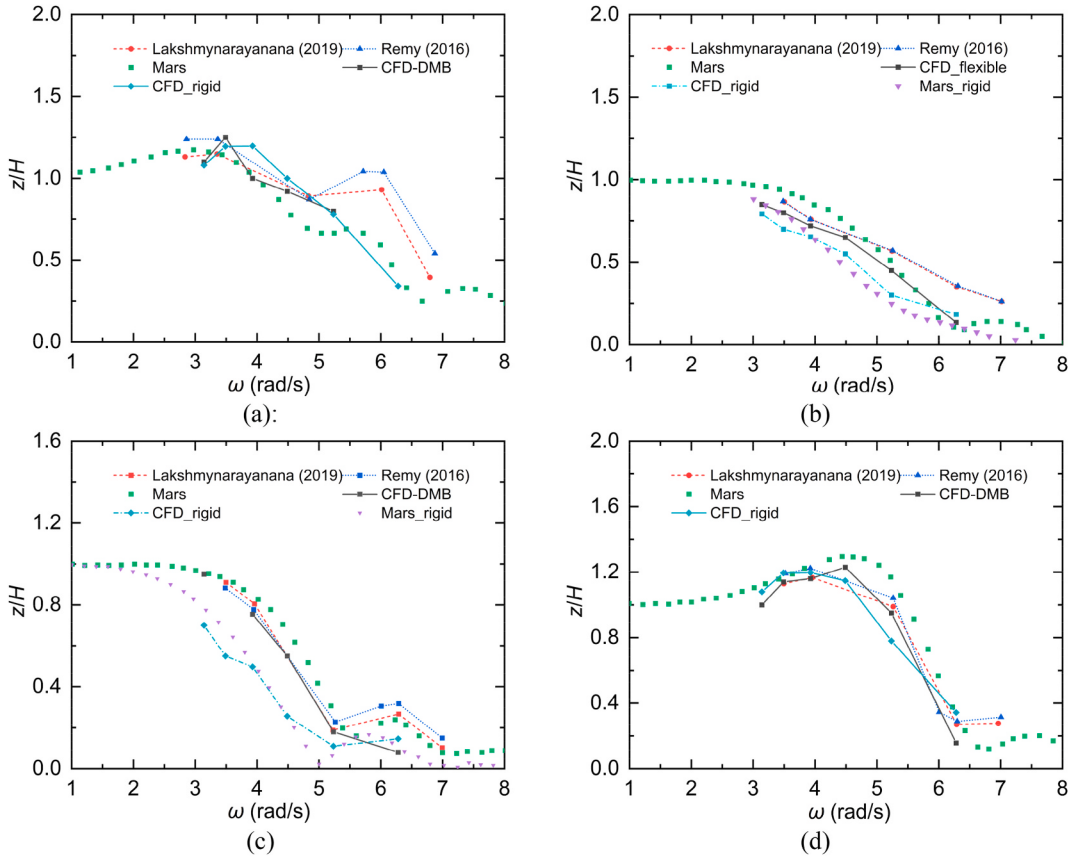


Fig. 11. Validation of heave displacements on VLFS sections in head waves: (a) Section #1 ($x/L = 0$), (b) Section #5 ($x/L = 0.4$), (c) Section #7 ($x/L = 0.5$), (d) Section #12 ($x/L = 1$).

transverse direction and 0.05 in the axial direction.

The numerical results are validated against the coupled OpenFOAM and MoorDyn method from Ref. [24] and experimental method from Ref. [25]. The computational time for the overset simulations (40 CPUs) is about 32 and 36 h for the two cases. Fig. 8 shows the structural dynamic motions of the VLFS, including heave (a), pitch (b) and surge (c). As it is shown in the figures that the numerical results are observed to converge with a mesh of 0.86 M. Fig. 8(c) and (d) demonstrate that some discrepancies are observed in pitch amplitude for both wave frequencies; however, the trend of the pitch curve generally shows good agreement between the present numerical results and those from Ref. [24]. The reason for these discrepancies may be related to the different mooring system principles employed. For example, the quasi-static mooring solver used in this study does not consider the hydrodynamic effects on the mooring lines, as was done in the previous work of [24]. Fig. 9 (a,b,c,d) displays the horizontal pull force component for the front and rear mooring lines under two wave conditions. The figures illustrate highly dynamic line tensions in both the front and rear lines, particularly in Fig. 9(b). Overall, there is good agreement between the experimental and numerical tension amplitudes for both the front and rear mooring lines.

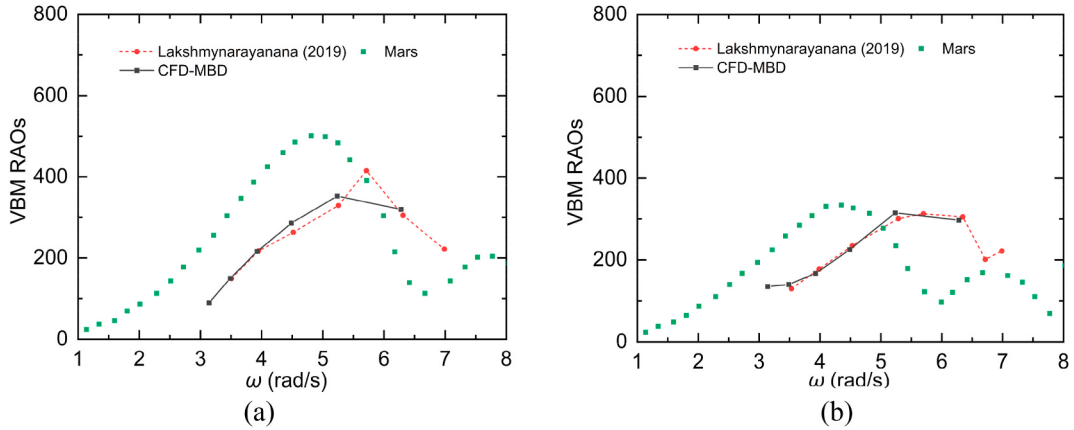


Fig. 12. RAOs of the vertical bending moments of the flexible VLFS in heading waves (a) Section #7 ($x/L = 0.5$), (b) Section #9 ($x/L = 0.66$).

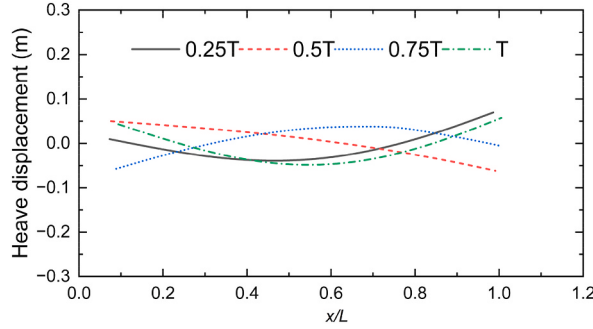


Fig. 13. Flexible VLFS shape at different time instants at the case of wave frequency $\omega_s = 3.925$ rad/s.

4. Results

4.1. Flexible VLFS in waves

The hydroelastic behaviours of a barge-shaped VLFS are first investigated in regular head waves based on the coupled CFD-DMB model. The physical and geometrical properties of the VLFS are in line with the experiments from Ref. [26]. The structure has a length of 2.28 m, a width of 0.6 m, and a depth of 0.25 m, as shown in Fig. 10 and the detailed configuration is summarised in Table 2. The mass of each section of the VLFS, which includes the sections, square rod, and bracing equipment, is aggregated as the analogous beam section mass and the lumped mass. No mooring system is equipped in this section. The hydrodynamic and hydroelastic data of the selected VLFS are available in open literature, such as experiments conducted by Ref. [26] and numerical studies by Ref. [10].

Fig. 11 compares the measured heave displacements at four VLFS sections (#1, #5, #7 and #12) against the experiments [27,28], Mars the 2D hydroelasticity theory [10], and coupled CFD-FEA model [10] for head waves with wave frequencies ranging from $\omega_s = 3.14$ rad/s to 6.28 rad/s. It can be observed that there is qualitative agreement between the experimental results and the present CFD-DMB method. Some discrepancies are observed in high-frequency wave range between the CFD-DMB method and the coupled CFD-FEA method. The reason for the differences observed could potentially be attributed to the development of different structural models from the multibody solver side. Such limitations were illustrated in these authors' previous papers [23] and [18]. Fig. 11(c) displays the global heave displacement for the rigid body case, and it exhibits good agreement with the rigid body results obtained from Mars.

From the numerical validation presented in these figures, it is clear that the present CFD-DMB method is capable of predicting the displacements of a very flexible structure to an acceptable degree of accuracy. When compared to linear methods (Mars), predictions that take into account nonlinearities are better suited for flexible structures that introduce significant free surface disturbances at certain frequencies. Omitting these nonlinearities can result in underpredictions when compared to actual measurements.

Fig. 12 shows the response amplitude operators (RAOs) of vertical bending moments (VBM), at location $x/L = 0.5$ and 0.66, along with comparisons from CFD-FEA and a 2D hydroelasticity study (Mars). Comparing the RAOs of VBM predicted by the CFD-FEA, it is seen that there is favourable agreement observed through all wave frequencies. However, the magnitudes of the calculated RAOs from both numerical methods show significant differences with the results from Mars at wave frequencies ranging from $\omega_s = 4.5$ –6 rad/s. The large difference in vertical bending moment may be due to the application of a large VBM on the VLFS when the wavelength is

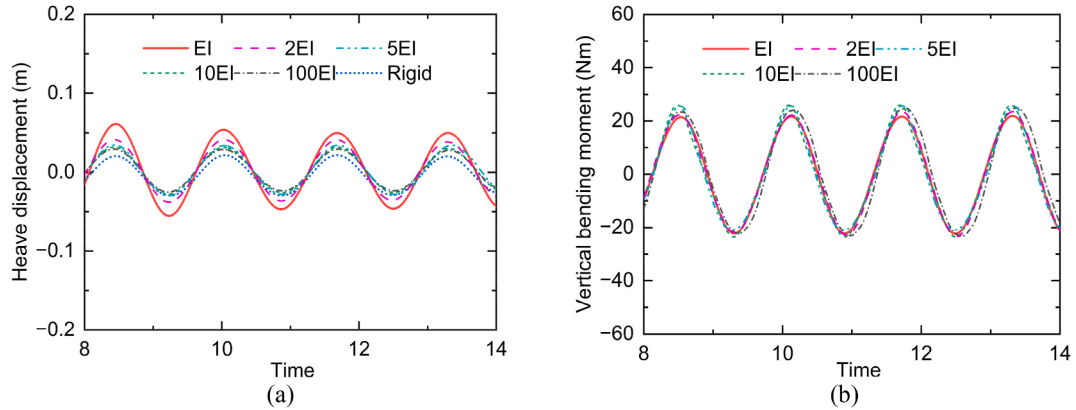


Fig. 14. Time domain analysis of six different VLFS stiffness on: (a) Mid-point VLFS heave displacement (m), (b) VBM (Nm) at amidship.

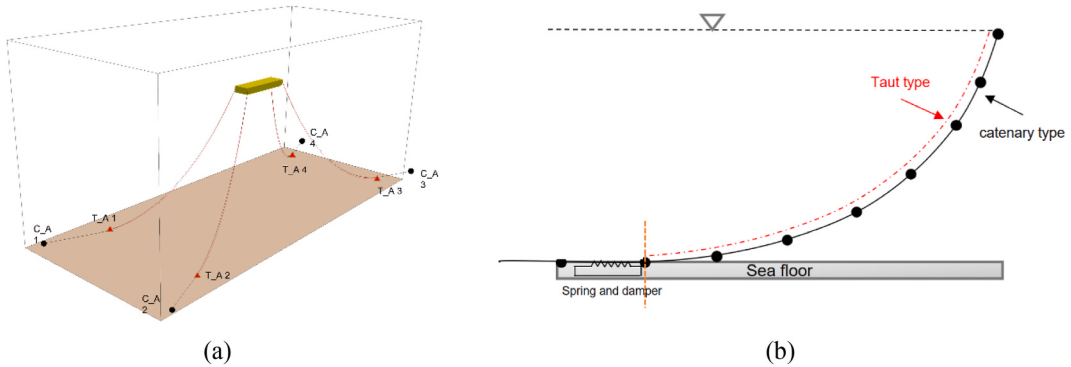


Fig. 15. The layout of the taut and catenary type of mooring lines (a) 3D demonstration, (b) 2D explanation.

equal to or near the characteristic length defined by the bending stiffness and the hydrostatic buoyancy coefficient [29]. Fig. 13 displays normalised deflection along the longitudinal sections of the VLFS in the wave frequency of $\omega_s = 3.925$ rad/s with four views in one complete wave cycle. It is evident that the structure underwent significant deformation during wave propagation.

An analysis is conducted to investigate the influence of six structural stiffnesses on the dynamic motions and internal loads of the VLFS for a head wave with a wave frequency of 3.925 rad/s, as shown in Fig. 14. In the model demonstration, the structural stiffness (EI) is increased multiple times while keeping the remaining parameters constant. The heave displacements and the VBM are extracted from the node close to the centre of gravity. The numerical results indicate that increasing the stiffness from EI to 100EI causes the structural responses to gradually become smaller and approach those of a rigid body case. These results are consistent with the stiffness theory in structural mechanics, which states that increasing stiffness can reduce the amount of deflection or bending in a flexible structure when it is subjected to a single frequency load. However, the effect on the maximum bending moments is less pronounced for the cases without mooring attached. According to the elastic beam bending equation $M = EI \frac{d^2w}{dx^2}$, where M is the bending moment, EI is the flexural rigidity, w is the deformation, bending moment is mainly dependent on the variation of E and w . In cases with changing stiffness, the deformation of the structure varies inversely, using the above equation, the bending moment at amidship has less influence on the structure's stiffness.

4.2. Coupling analysis between mooring and structure hydroelasticity

The coupled effects of the structural hydroelasticity and loose-type mooring system are evaluated in this section. Two different mooring line designs, i.e., taut, and catenary mooring lines, are employed to connect between the flexible structure with the seabed, as shown in Fig. 15. Two pairs of fairleads are tied at four corners on VLFS sections (#1, #12), as shown in Fig. 15(a).

Each mooring line consists of 40 segments representing its elastic behaviour. The catenary mooring lines have a line profile that lies partly on the seabed in the static equilibrium position, which generates the necessary compliance to cope with structures dynamic motions. In contrast, taut mooring lines maintain a taut condition by applying a specific amount of pretension on both ends of the cable. Unlike catenary mooring, there are no line segments lying on the seabed.

In this study, the taut mooring system is designed with the same hanging length as the catenary mooring, which means the taut anchor points are consistent with the catenary lying position, as shown in 2D in Fig. 15(b). The 3D demonstration is shown in Fig. 15

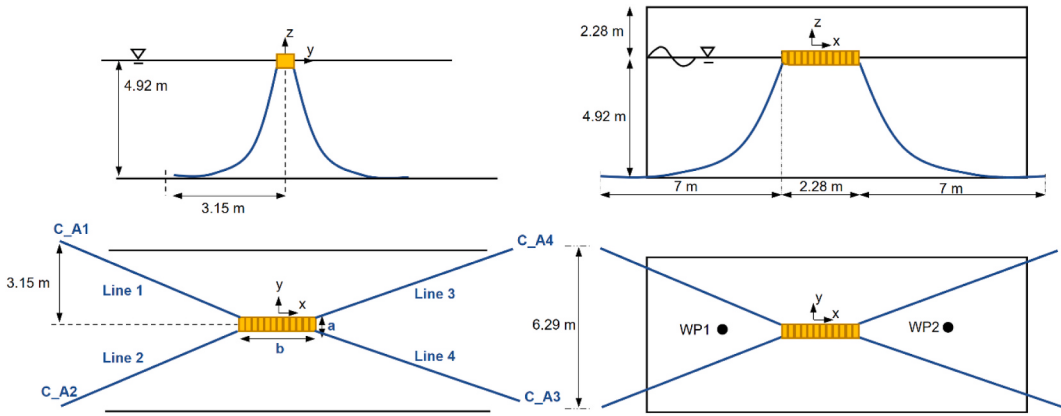


Fig. 16. The catenary mooring layout.

Table 3
Catenary and taut type of mooring characteristics.

Mooring type	Catenary	Taut
Anchor positions (m) (C_A, T_A)	(-7 -3.19–4.92), (-7 3.19–4.92), (9.25–3.19 -4.92), (9.25 3.19–4.92)	(-5 -2.4 -4.92), (-5 2.4–4.92), (7.25–2.4 -4.92), (7.25 2.4–4.92)
Fairlead positions (m)	(0.01–0.3 0.013), (0.01 0.3 0.013) (2.25–0.3 0.013), (2.25 0.3 0.013)	
Mooring length (m)	9.5	7.7
Arrangement angles (°)	45°, 135°, 225°, 315°	
Mooring Segments number	40	
Lied down segment number	8	0
Seabed Stiffness (N/m)	6e ⁶	
Mooring weight in water per unit mass (kg/m)	1.135	
Mooring Young modulus (N/m)	1.63529 e ⁷ , 1.63529 e ⁸ , 1.63529 e ⁹ ,	
Mooring lines diameter (m)	0.0766	
Pre-tension force on catenary mooring (N)	88.03	
Pre-tension force on taut mooring (N)	120.05	

(a), the red lines indicate taut mooring (T_c) and the black lines are catenary mooring (C_c). The pair of mooring lines close to the wave maker is denoted as front (A₁, A₂) and the one far away from the wave maker is denoted as rear (A₃, A₄). The anchoring positions of taut mooring are calculated based on the catenary equations. By designing it this way, it is possible to ensure that the mooring forces at the initial stage are similar between the taut and catenary cases. The mooring arrangements are shown in Fig. 16 and physical properties are summarised in Table 3.

4.2.1. 1: influence of mooring system on to structure hydroelasticity

This section delves into a comprehensive study that explores the impact of the mooring lines on the hydroelastic behaviours of the structure. Catenary and taut type of mooring lines with various mooring stiffness values are evaluated on the dynamic motions of the hydro-elastic-moored model. The presented results include vertical motions, VBM_s, and tension forces acting on the mooring lines.

4.2.1.1. The influences of mooring types on the structure hydroelasticity. This section compares the effect from attaching taut or catenary type of mooring lines on the dynamic motions of VLFS with the consideration of the structural hydroelasticity.

Fig. 17(a) shows the time trajectory of the vertical plane motion extracted at the midship of the VLFS for no mooring, catenary and taut mooring cases. The signals from mooring cases display circular shapes with repeat cycles that result from the movements of the structure following with wave particle motions. It is seen that heave motions by the cases of taut and catenary mooring are similar, but the structure is offered more in surge motions by equipping catenary mooring lines. This is because taut mooring lines apply the tension forces to the structure to avoid its drift in waves. As compared to cases with no mooring, it has been found that the heave displacement at the longitudinal of VLFS can be reduced when equipping with mooring lines, as evidenced by Ref. [13].

Fig. 17(b) shows the vertical heave displacements at section #1 for cases with/without moorings. It is seen that by attaching a mooring system to flexible structure will cause the front section to sink because of the extra weight. For case with catenary exhibits slightly larger motions, with a 15% increase compared to the taut case. The reason for this is that catenary mooring relies mainly on the gravity from the lying down part of the mooring, while taut mooring has tension restraints directly from anchor points.

The maximum VLFS_s and VBM_s from the cases with taut/catenary mooring types are extracted from each VLFS sections and

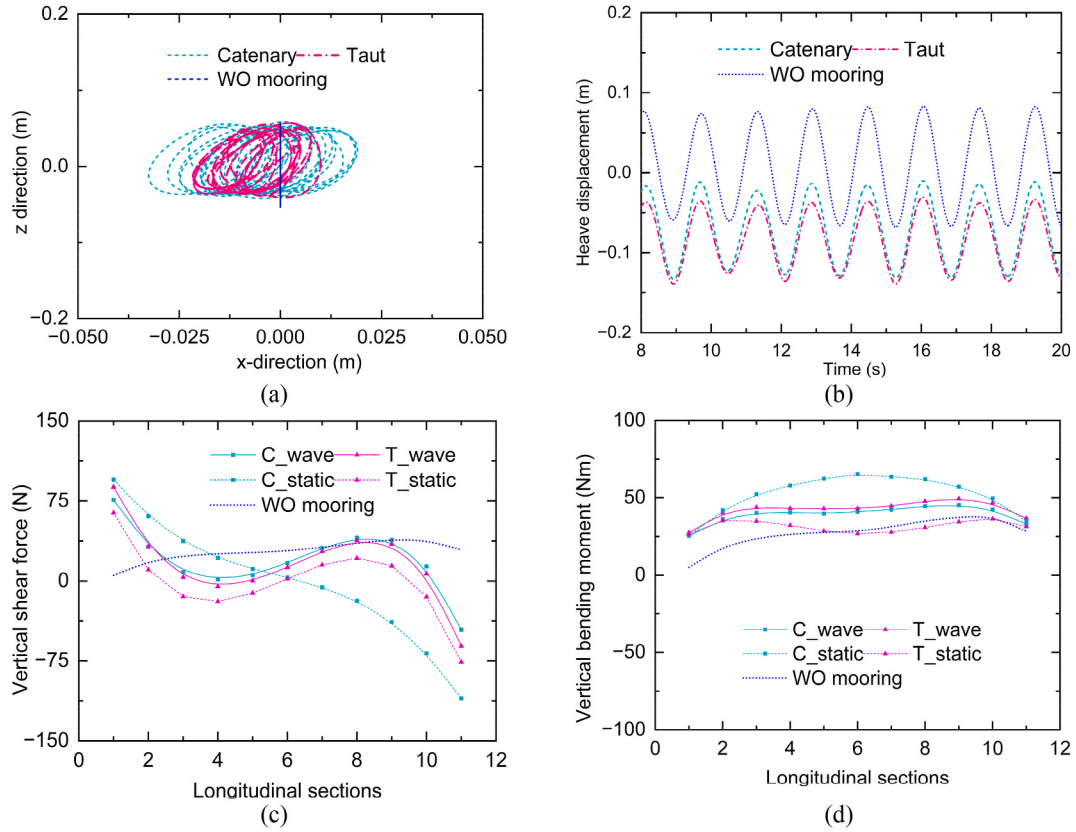


Fig. 17. The comparison between catenary and taut moorings lines (a) Time trajectory of the vertical plane motion extracted from the centre mass point of the VLFS ($x/L = 0.5$), (b) Time history records on the front section #1, (c) longitudinal VSF distributions, (d) Longitudinal VBMs distributions.

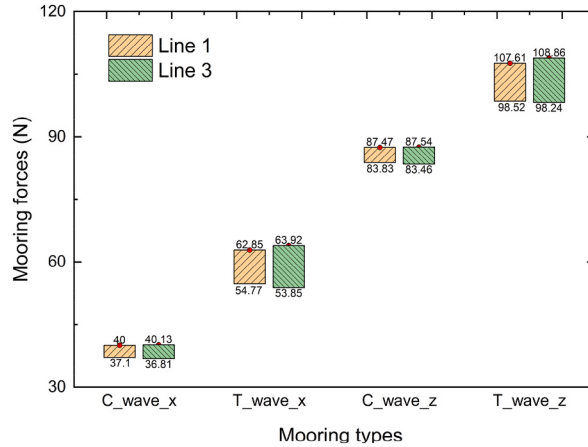


Fig. 18. The mooring tensional forces comparison between the catenary and taut mooring lines.

compared between those with/without mooring at static water/wave (shown in Fig. 17(c and d)). When compared to the no mooring cases, it is evident that the sectional loads at fairlead sections change significantly. It is seen that the VBMs at front section #1 raises from 4.92Nm in no mooring case to 26.4Nm in catenary and taut mooring cases.

The static case calculates the sectional loads of the VLFS in calm water, as shown in Fig. 17(d). It is seen that the structure stays in a permanent hogging shape with the catenary mooring (C_static) due to added weights onto two ends. The maximum hogging moments of the C_static case are detected at section #6 with a magnitude of 65.27Nm. The value is reduced to 41 Nm when considering the catenary case in waves, which can be attributed to the buoyancy compensation provided by the waves.

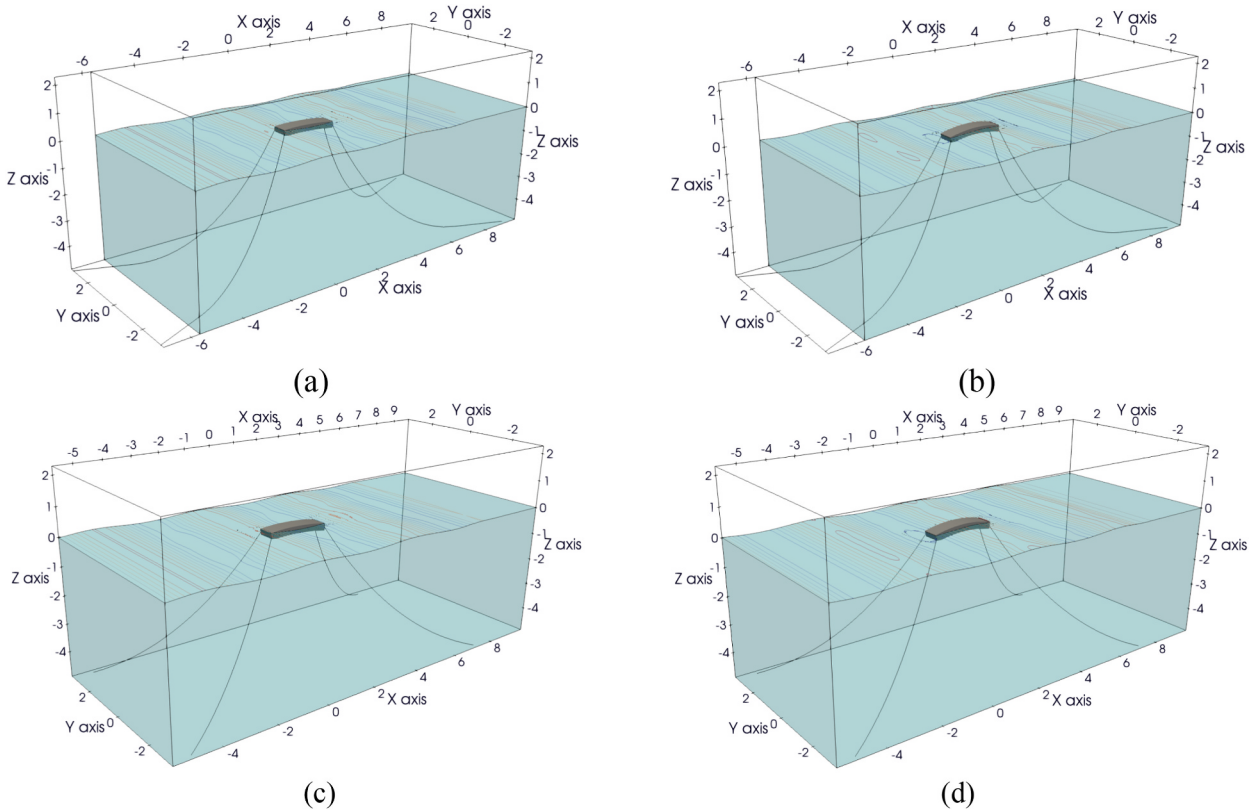


Fig. 19. Virtual observation of the fluid field with taut/catenary with two views in one wave cycle (a) Catenary mooring case in time 9s, (b) Catenary mooring case in time 10.5s, (c) Taut mooring case in time 9s and (d) Taut mooring case in time 10.5s.

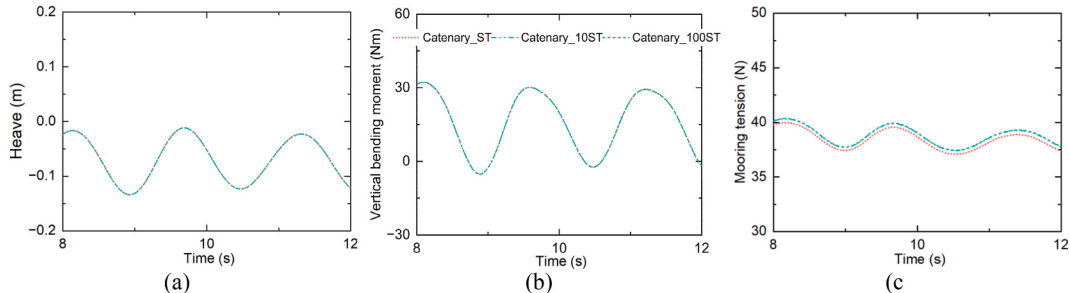


Fig. 20. Comparison on three catenary mooring stiffness on (a) Heave displacement at front section #1, (b) VBM_s at amidship section, (c) Mooring tensional force at line 1.

The VLFS with taut mooring in calm water (T_{static}) shows a relative sagging shape (Fig. 17(d)) because the taut mooring not only induces gravity forces but also the pre-tensional forces onto the structure. The pre-tension forces drag the structure downward and distribute the force evenly to near segments without a local high peak VBM_s occurs. This finding indicates that taut mooring lines are more suitable for this VLFS in calm water, and both taut and catenary moorings have similar performance in wave conditions.

The longitudinal wave-induced VBM_s distribution of both taut (T_{wave}) and catenary (C_{wave}) mooring cases in waves show a similar trend. The peak hogging moments for both mooring types are detected at section #3 and #9, as shown in Fig. 17(d). The changes are smooth towards the midship and the largest sagging moments are found 39.7Nm at section #5 for catenary case and 42.9Nm for taut cases. It can be concluded that attaching a mooring system to a slender, deformable structure has a significant effect on its hydroelasticity characteristics. By carefully selecting the mooring types and parameters, it is possible to reduce the local maximum VBM_s and protect the structure from breaking apart.

Fig. 18 shows the cases of catenary and taut mooring lines with waves under the maximum tension forces in the horizontal (x) and vertical (z) directions. From the figure, it can be seen that due to the symmetrical mooring arrangement, the tension fluctuations of Line1 and Line3 are basically the same. Taut type mooring lines generally have greater tension than catenary type, and the tension in

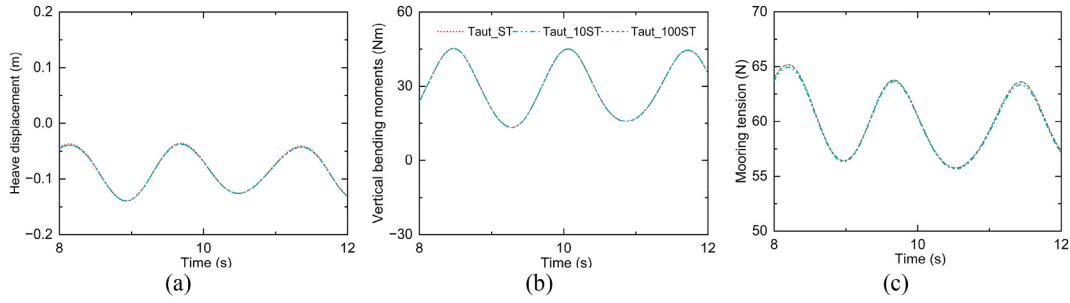


Fig. 21. Comparison on three taut mooring stiffness on (a) Heave displacement at front section #1, (b) VBM at amidship section, (c) Mooring tensional force at line 1.

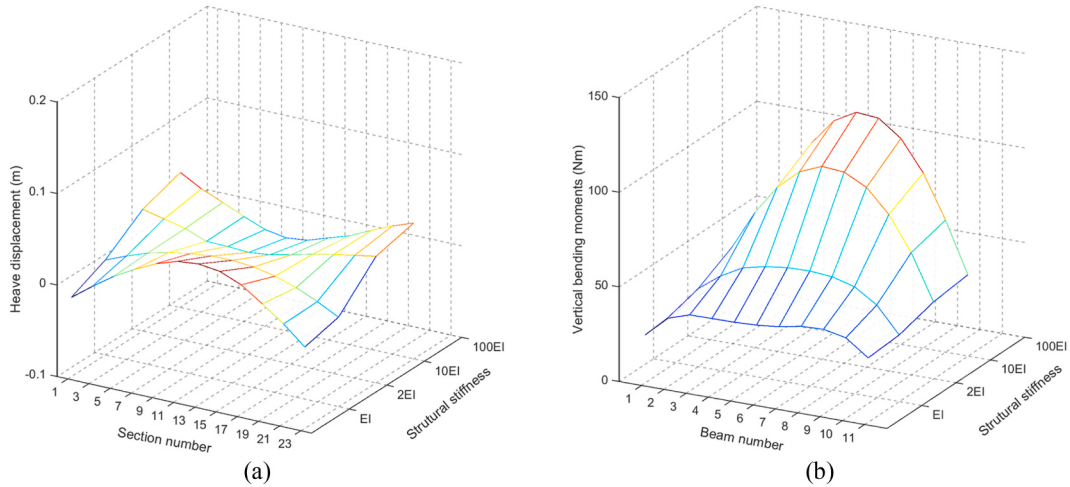


Fig. 22. Comparison of four mooring stiffness on (a) The vertical displacement, (b) Longitudinal VBM distributions.

the z direction will be greater than that in the x-axis direction due to the structural gravity.

Fig. 19 displays two views of the virtual observation of the hogging and sagging behaviours with catenary or taut mooring lines over one wave cycle for a wave frequency of $\Omega_s = 3.925\text{rad/s}$. The figures reveal similar global structural motion and deformation in both cases. However, the flow field in the catenary mooring case displays more obvious radiated waves due to larger vertical motions compared to the taut mooring case.

4.2.1.2. The influences of mooring stiffness on the structure hydroelasticity. The mooring line stiffness for both catenary and taut types is evaluated to determine its influence on the hydroelastic characteristics of the VLFS. For this purpose, a parametric study is carried out with three different mooring line stiffness, ranging from 1 ST ($1.635e^7$) to 100 ST ($1.635e^9$). The other model settings remain the same, with a wave condition selected at a frequency of $\omega_s = 3.925\text{rad/s}$ and a wave height of $H_s = 0.10\text{m}$. Fig. 20(a) and Fig. 21(a) show the dynamic heave motion at VLFS section #1 for three mooring line stiffnesses between catenary and taut mooring types. The VBM extracted from the amidship is shown in Figs. 20(b) and Fig. 21(b) for both mooring types. The horizontal mooring force of the catenary and taut type mooring at line 1 is shown in Figs. 20(c) and Fig. 21(c).

It can be seen from the figures that the structural motions and VBM of both catenary and taut cases are not sensitive with mooring stiffness. Only a small difference appears in the forces from catenary mooring as shown in Fig. 20(c). Therefore, it can be concluded that increasing the stiffness of the catenary mooring lines has little influence on the hydroelasticity of the structure. The tensions on the mooring lines are also compared, and negligible differences are found among each case.

4.2.2. The influences of structure hydroelasticity on mooring lines

This section presents a comprehensive study that investigates the impact of structural hydroelasticity on catenary type mooring lines. Four different VLFS stiffness, ranging from EI to 100EI, are evaluated accordingly. The numerical results, including the dynamic motions of the hydro-elastic-moored model and the tension forces in time domain are presented. The selected wave frequency is $\omega_s = 3.925\text{rad/s}$ with a wave height of $H_s = 0.10\text{m}$, representing a medium-long wave which is applied throughout all cases.

4.2.2.1. Dynamic motions and bending loads. Fig. 22(a) shows 3D plots of longitudinal heave displacements for each VLFS sections with

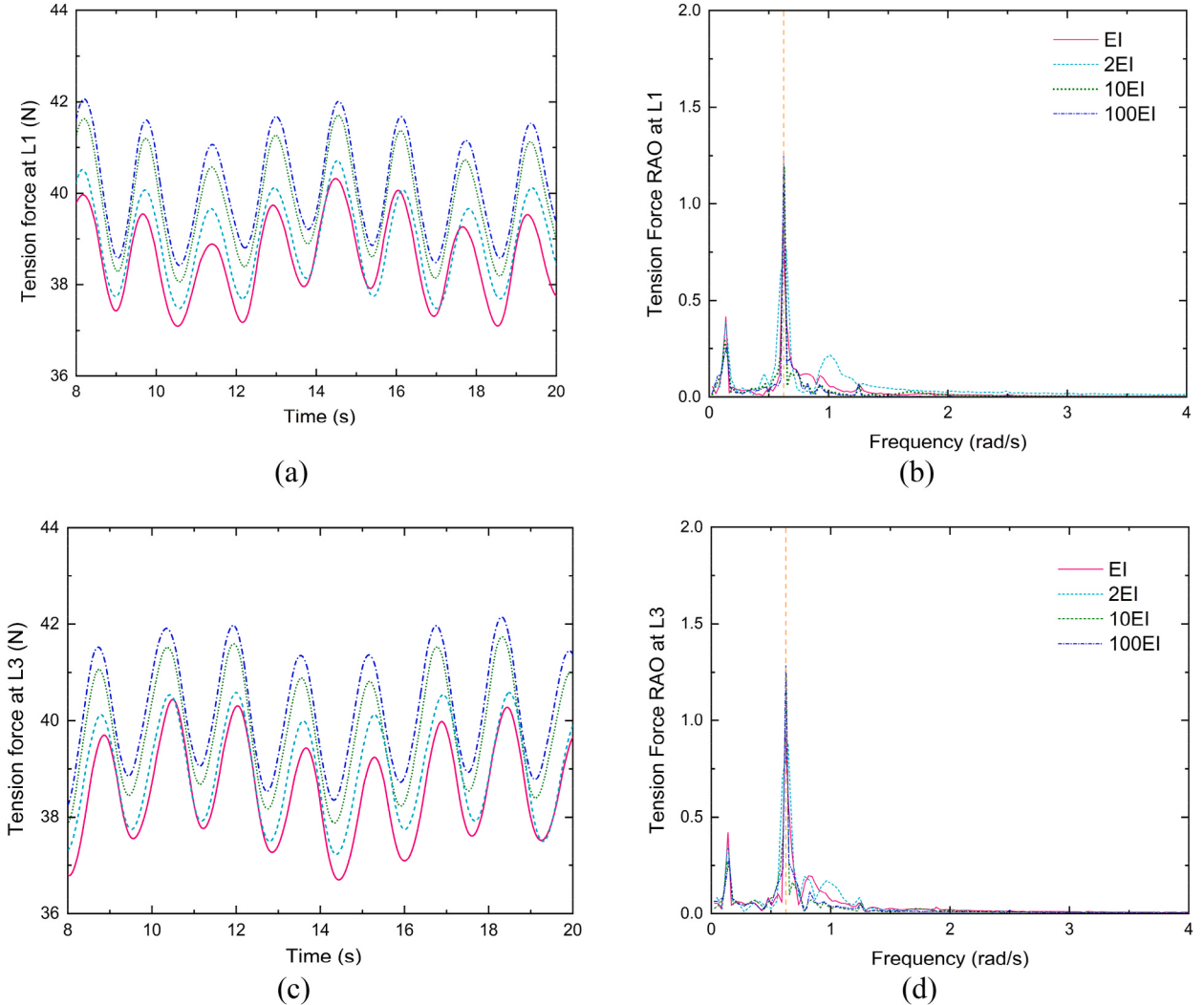


Fig. 23. Horizontal mooring forces evaluated through four structural stiffness taut and catenary in wave frequency $\omega_s = 3.925 \text{ rad/s}$: (a) Tension force at L1x, (b) FFT analysis on L1x tension force, (c) Tension force at L3x and (d) FFT analysis on L3x tension force.

respect to four structural stiffness values (EI, 2EI, 10EI, and 100EI). With an increase in the stiffness of a moored-flexible VLF, the longitudinal heave motions undergo significant changes. Specifically, the deflection amplitudes at the middle section become smaller, but the motions at the two ends become larger. This is because an increase in stiffness alters the structural flexural characteristics, causing the rigid body state to dominate. As a result, global pitch motion leads to large displacements at both ends.

Fig. 22(b) shows a 3D plot of longitudinal VBM_s extracted from each VLFS section, compared with four structural stiffness. The figure indicates that changes in structural stiffness have a significant effect on longitudinal VBM_s. As the structural stiffness increases from EI to 100EI, the hogging moment at the middle section (#6) gradually increases from 40.92Nm to 118.5Nm.

When compared to the no-moored cases shown in Fig. 14(b), the VBM_s of cases with catenary mooring lines increase drastically following with the structure stiffness. This is because the mooring system acts as a “soft” boundary condition, restraining the flexible structure by applying a force at two ends. These forces will cause a high VBM_s at amid sections and the magnitude of VBM_s increase with the stiffness of the structure. This previously unreported finding notices that slender and stiff structures attached with catenary moorings will experience larger VBM_s at the amid section. A carefully designed mooring system is required, especially for stiff structures, to avoid the possibility of breakage.

4.2.2.2. Mooring forces. Figs. 23 and 24 show the time-series tension forces at line 1 and line 3 at horizontal (x) and vertical directions (z) with four structural stiffness from EI to 100EI. The front mooring lines provide forces acting in the opposite direction to the wave propagation, and they experience tension forces similar to those acting on the rear lines. Table 4 summarises the peak tension forces for all structure stiffness in two directions. It can be observed that the elastic deflections of the VLFS significantly contribute to the tension forces in the mooring lines. The magnitudes of tension forces increase by 6% for all directions as the flexural rigidity of the VLFS

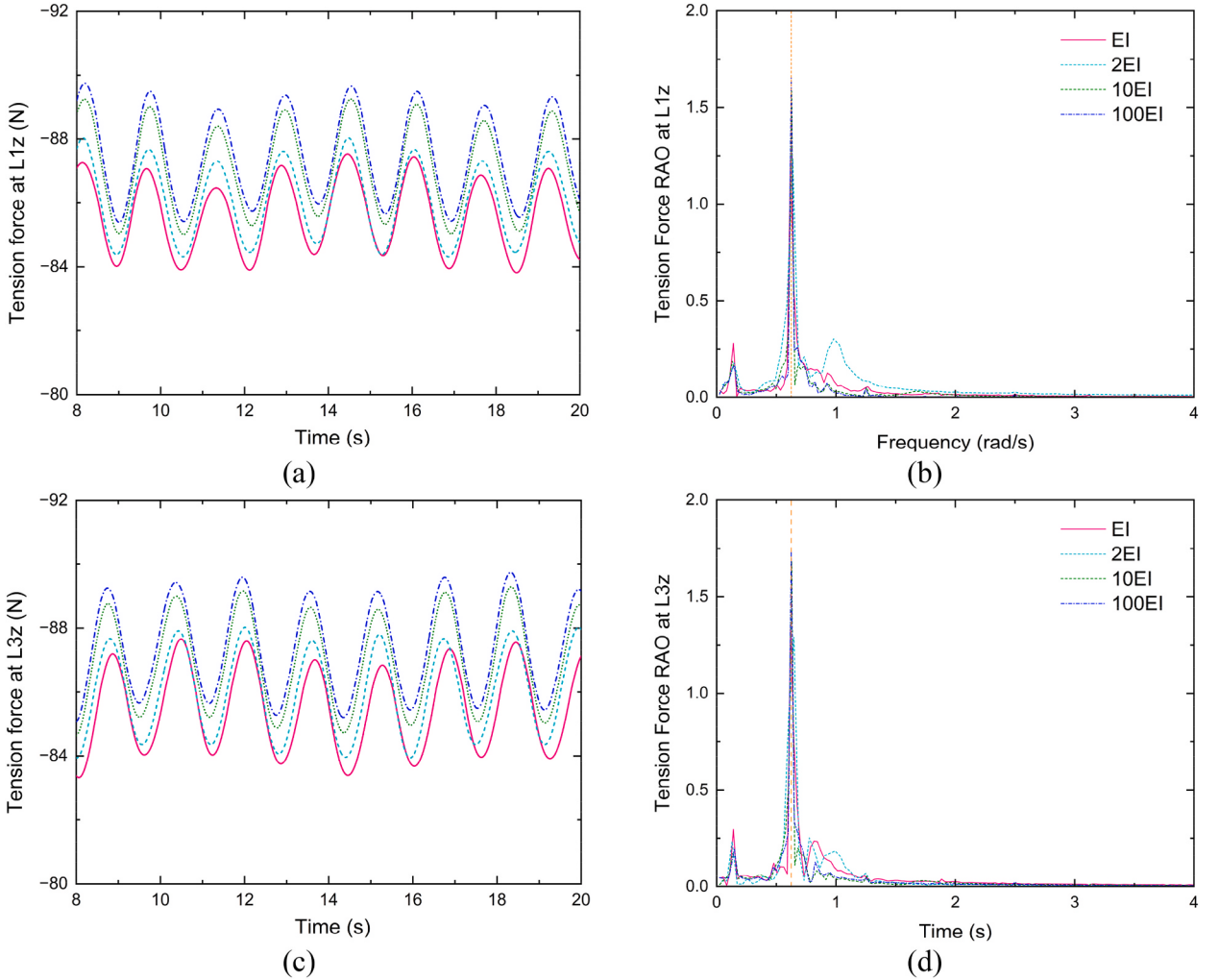


Fig. 24. Vertical mooring forces evaluated through four structural stiffness taut and catenary in wave frequency $\omega_s = 3.925 \text{ rad/s}$: (a) Tension force at L1z, (b) FFT analysis on L1z tension force, (c) Tension force at L3z and (d) FFT analysis on L3z tension force.

Table 4

Tension peak value on the x and z directions of L1 and L3 mooring lines.

Structural stiffness	Tension_L1x (N)	Tension_L3x (N)	Tension_L1z (N)	Tension_L3z (N)
EI (Nm)	40.3	40.27	-87.5	-87.6
2EI (Nm)	40.7	40.55	-88.0	-87.9
10EI (Nm)	41.7	41.7	-89.2	-89.3
100EI (Nm)	42.0	42.1	-89.7	-89.7

increases from EI to 100EI.

The time series results are further evaluated based on Fast Fourier Transform (FFT), as shown in Figs. 23(a) and Fig. 24(b). Two resonant frequencies can be observed in the figure: the primary frequency coincides with the incident wave frequency (depicted by orange dots), while the other corresponds to the mooring lines. The amplitude of the first frequency decreases with the increase of structural stiffness, while the amplitude of the second frequency increases. A series of small amplitude frequencies are also present, which may be induced by the limitations of the present method that introduce spurious frequencies through the addition of constraints boundary conditions into the Lagrange equations.

Fig. 25 compares the virtual observation of structural deformation and fairlead positions at time $t = 12.5\text{s}$ for two different structure stiffnesses (EI in colour and 100EI in grey). In the case of 100EI, the structure is grey with an attached red catenary mooring, while in the case of EI, the structure is coloured with a black mooring attached. The figure shows that the fairleads move with the mooring sections due to local rigid body motions. As a result, the tension force/moment of each mooring line will pass to the

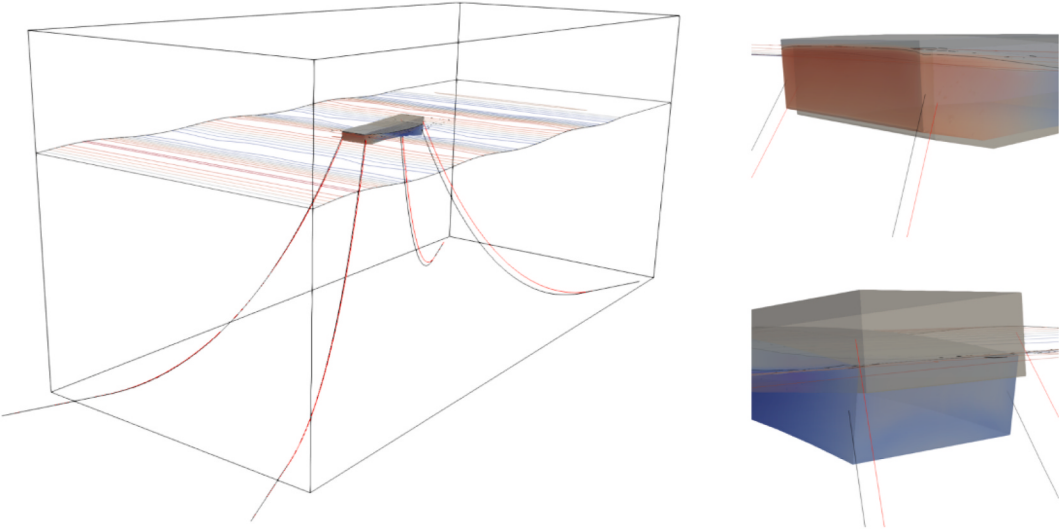


Fig. 25. Virtual observations of the structure and mooring updates between EI and 100EI.

corresponding rigid patch as a boundary condition to restrain the flexible structure's movements.

5. Conclusions

This paper introduces a novel numerical framework that integrates a quasi-static mooring solver into a two-way CFD-DMB framework to investigate the coupling effects between the structural hydroelasticity and loose-type (catenary and taut) mooring systems of a deformable VLFS in waves. In particular, OpenFOAM is used as the CFD solver, while MBDyn is chosen as the structure solver to calculate the elastic behaviours of the flexible VLFS.

The validations of mooring models and flexible structures show good agreement with previous simulations and experiments. The performance of mooring codes is validated by first using a benchmark case: a simple floating box restrained by catenary mooring in waves. The dynamic motions and mooring tension forces are evaluated at two wave frequencies, showing acceptable agreement with the experiments and coupled OpenFOAM&MoorDyn models. Next, the hydroelastic behaviours of the flexible VLFS without mooring in waves are evaluated using the present CFD-DMB model. The numerical results, including heave displacements and internal loads at longitudinal VLFS sections, show favourable agreement with the numerical results from CFD-FEA and the experiments. An analysis is conducted to investigate the influence of six structural stiffnesses on the dynamic motions and internal loads of the VLFS in a heading wave frequency. The numerical results indicate that increasing the stiffness from EI to 100EI causes the structural responses to gradually become smaller and approach those of rigid body state.

The coupled effects of the structural hydroelasticity and loose-type mooring system are evaluated. The main conclusions are outlined below.

- Attaching a loose-type mooring system to a slender, deformable structure drastically changes the hydrodynamic and hydroelastic behaviours of the flexible VLFS. It has been found that the longitudinal deflections of the VLFS are reduced by equipping a mooring. However, the sections at the two ends will sink due to the added weight at the fairlead positions. Cases with catenary mooring exhibit slightly larger motions in the vertical plane (i.e., surge and heave) compared to the taut case.
- Equipping the loose type mooring system changes the flexural characteristics of the VLFS, including the static and wave-induced VBM distributions. The structure with the catenary mooring shows a hogging shape in calm water, with the peak is detected at middle section #6. In contrast, the case with taut mooring distributes the loads evenly to near sections, without any localized high peak VBMs. The results from wave-induced VBMs show that both catenary and taut case have peak hogging moments detected at section #3 and #9 (shown in Fig. 17(d)). However, mooring stiffness have less influences on the flexible structure motions in this study.
- On the other hand, the hydroelastic behaviours also have significant impact on the mooring system. The dynamic motions of the hydro-elastic-moored model and the tension forces are evaluated with four structural stiffness. It is observed that the deflection amplitudes at the middle sections of the flexible VLFS become smaller as the stiffness of the structure increases, but the motions at the two ends become larger. This increase is also accompanied by a significant increase in the VBMs, especially at the middle sections (#4~#8) of the VLFS.

The proposed hydro-elastic-mooring framework has great flexibility to extend its applications to other marine structures, such as evaluating the hydroelasticity of moored ships in waves. However, the present method is constrained by the Euler-beam approach, which cannot accurately capture large torsional deformations. This issue emphasizes the necessity for future work, which involves

implementing a high-order beam theory, such as the Vlasov beam, to replace the traditional Euler-Bernoulli beam. This new approach would also consider the cross-sectional warping effects. Our future endeavours will focus on addressing this aspect and further elucidating the coupling effects between a full-scale elastic VLFS and the mooring system.

Credit authors statement

Yujia Wei: Conceptualization, Methodology, Formal analysis, Writing – original draft. **Shuangrui Yu:** Conceptualization, Writing – review & editing, **Peng Jin:** Writing – review & editing, **Luofeng Huang:** review & editing, **Khaled Elsherbiny:** review & editing, **Tahsin Tezdogan:** Conceptualization, Writing – review & editing, supervision.

Declaration of competing interest

The authors declare that they have no known competing financial interests or personal relationships that could have appeared to influence the work reported in this paper.

Data availability

No data was used for the research described in the article.

Acknowledgments

The authors would like to acknowledge the numerical results were obtained using the ARCHIE-WeSt High Performance Computer (www.archie-west.ac.uk) based at the University of Strathclyde.

References

- [1] Lamas-Pardo M, Iglesias G, Carral L. A review of very large floating structures (VLFS) for coastal and offshore uses. *Ocean Eng* 2015;109:677–90.
- [2] Wang C, Tay Z. Very large floating structures: applications, research and development. *Procedia Eng* 2011;14:62–72.
- [3] Watanabe E, Utsunomiya T, Wang CM. Hydroelastic analysis of pontoon-type VLFS: a literature survey. *Eng Struct* 2004;26(2):245–56. <https://doi.org/10.1016/j.engstruct.2003.10.001>.
- [4] Loukogeorgaki E, Yagci O, Kabdasli MS. 3D Experimental investigation of the structural response and the effectiveness of a moored floating breakwater with flexibly connected modules. *Coast Eng* 2014;91:164–80.
- [5] Loukogeorgaki E, Lentsiou EN, Aksel M, Yagci O. Experimental investigation of the hydroelastic and the structural response of a moored pontoon-type modular floating breakwater with flexible connectors. *Coast Eng* 2017;121:240–54. <https://doi.org/10.1016/j.coastaleng.2016.09.002>.
- [6] Jin C, Bakti FP, Kim M. Multi-floater-mooring coupled time-domain hydro-elastic analysis in regular and irregular waves. *Appl Ocean Res* 2020;101. <https://doi.org/10.1016/j.apor.2020.102276>.
- [7] Bakti FP, Jin C, Kim MH. Practical approach of linear hydro-elasticity effect on vessel with forward speed in the frequency domain. *J Fluid Struct* 2021;101. <https://doi.org/10.1016/j.jfluidstructs.2020.103204>.
- [8] Lu D, Fu S, Zhang X, Guo F, Gao Y. A method to estimate the hydroelastic behaviour of VLFS based on multi-rigid-body dynamics and beam bending. *Ships Offshore Struct* 2016;14(4):354–62. <https://doi.org/10.1080/17445302.2016.1186332>.
- [9] Zhang X, Lu D, Gao Y, Chen L. A time domain discrete-module-beam-bending-based hydroelasticity method for the transient response of very large floating structures under unsteady external loads. *Ocean Eng* 2018;164:332–49.
- [10] Lakshmynarayanan PA, Temarel P. Application of CFD and FEA coupling to predict dynamic behaviour of a flexible barge in regular head waves. *Mar Struct* 2019;65:308–25. <https://doi.org/10.1016/j.marstruc.2019.02.006>.
- [11] Jiang C, el Moctar O. Extension of a coupled mooring-viscous flow solver to account for mooring-joint-multibody interaction in waves. *Journal of Ocean Engineering and Marine Energy* 2022;9(1):93–111. <https://doi.org/10.1007/s40722-022-00252-z>.
- [12] Nguyen HP, Dai J, Wang CM, Ang KK, Luong VH. Reducing hydroelastic responses of pontoon-type VLFS using vertical elastic mooring lines. *Mar Struct* 2018;59:251–70. <https://doi.org/10.1016/j.marstruc.2018.02.005>.
- [13] Ni X, Cheng X, Wu B, Wang X. Coupled analysis between mooring system and VLFS with an effect of elastic deflection of floater. *Ocean Eng* 2018;165:319–27. <https://doi.org/10.1016/j.oceaneng.2018.07.044>.
- [14] Mohapatra SC, Soares CG. Effect of mooring lines on the hydroelastic response of a floating flexible plate using the BIEM approach. *J Mar Sci Eng* 2021;9(9). <https://doi.org/10.3390/jmse9090941>.
- [15] Bispo IBS, Mohapatra SC, Guedes Soares C. Numerical analysis of a moored very large floating structure composed by a set of hinged plates. *Ocean Eng* 2022;253. <https://doi.org/10.1016/j.oceaneng.2022.110785>.
- [16] Hirt CW, Nichols BD. Volume of fluid (VOF) method for the dynamics of free boundaries. *J Comput Phys* 1981;39(1):201–25.
- [17] Jacobsen NG, Fuhrman DR, Fredsøe J. A wave generation toolbox for the open-source CFD library: OpenFoam. *Int J Numer Methods Fluid* 2012;70(9):1073–88. <https://doi.org/10.1002/fld.2726>.
- [18] Wei Y, Incecik A, Tezdogan T. A hydroelasticity analysis of a damaged ship based on a two-way coupled CFD-DMB method. *Ocean Eng* 2023;274:114075.
- [19] Maserati P, Morandini M, Mantegazza P. An efficient formulation for general-purpose multibody/multiphysics analysis. *J Comput Nonlinear Dynam* 2014;9(4). <https://doi.org/10.1115/1.4025628>.
- [20] Ghiringhelli GL, M P, Mantegazza P. Multibody implementation of finite volume C beams. *AIAA J* 2000;38(1):131–8. <https://doi.org/10.2514/2.933>.
- [21] Ong PP, Pellegrino S. Modelling of seabed interaction in frequency domain analysis of mooring cables. In: Paper presented at the international conference on offshore mechanics and arctic engineering; 2003.
- [22] Liu Y, Xiao Q, Incecik A, Peyrard C. Aeroelastic analysis of a floating offshore wind turbine in platform-induced surge motion using a fully coupled CFD-MBD method. *Wind Energy* 2019;22(1):1–20.
- [23] Wei, Incecik A, Tezdogan T. A fully coupled CFD-DMB approach on the ship hydroelasticity of a containership in extreme wave conditions. *J Mar Sci Eng* 2022;10(11):1778.
- [24] Chen H, Hall M. CFD simulation of floating body motion with mooring dynamics: coupling MoorDyn with OpenFOAM. *Appl Ocean Res* 2022;124. <https://doi.org/10.1016/j.apor.2022.103210>.
- [25] Domínguez JM, Crespo AJC, Hall M, Altomare C, Wu M, Stratigaki V, Gómez-Gesteira M. SPH simulation of floating structures with moorings. *Coast Eng* 2019;153. <https://doi.org/10.1016/j.coastaleng.2019.103560>.

- [26] Senjanović I, M Š, Tomas S. Investigation of ship hydroelasticity. *Ocean Eng* 2008;35(5–6):523–35. <https://doi.org/10.1016/j.oceaneng.2007.11.008>.
- [27] Senjanović I, M Š, Tomašević S. Hydroelasticity of large container ships. *Mar Struct* 2009;22(2):287–314. <https://doi.org/10.1016/j.marstruc.2008.04.002>.
- [28] Remy F, Molin B, Ledoux A. Experimental and numerical study of the wave response of a flexible barge. In: *Hydroelasticity in marine technology*; 2006. p. 255–64. Wuxi, China.
- [29] Suzuki H, Yoshida Koichiro, Iijima aK. A consideration of the structural design of a large-scale floating structure. *J Mar Sci Technol* 1996:255–67.